
Article:
Cavill, Stuart Alan orcid.org/0000-0002-1359-4958, Huang, Chunli, Offidani, Manuel orcid.org/0000-0002-3500-8198 et al. (3 more authors) (2020) Proposal for Unambiguous Electrical Detection of Spin-Charge Conversion in Lateral Spin Valves. Physical Review Letters. 236803. ISSN 1079-7114

https://doi.org/10.1103/PhysRevLett.124.236803

Proposal for Unambiguous Electrical Detection of Spin-Charge Conversion in Lateral Spin Valves

Stuart A. Cavill,[1] Chunli Huang,[2,3] Manuel Offidani,[1] Yu-Hsuan Lin,[2] Miguel A. Cazalilla,[2,4,5] and Aires Ferreira[1,*]

[1]*Department of Physics, University of York, YO10 5DD York, United Kingdom*

[2]*Department of Physics, National Tsing Hua University and National Center for Theoretical Sciences (NCTS), Hsinchu 30013, Taiwan*

[3]*Department of Physics, The University of Texas at Austin, Austin, Texas 78712, USA*

[4]*Donostia International Physics Center (DIPC), Paseo Manuel de Lardizabal, 4, 20018 Donostia, Spain*

[5]*Yukawa Institute for Theoretical Physics, Kyoto University, Kyoto 606-8502, Japan*

(Received 28 June 2019; revised manuscript received 9 March 2020; accepted 12 May 2020; published 11 June 2020)

Efficient detection of spin-charge conversion is crucial for advancing our understanding of emergent phenomena in spin-orbit-coupled nanostructures. Here, we provide a proof of principle of an electrical detection scheme of spin-charge conversion that enables full disentanglement of competing spin-orbit coupling (SOC) transport phenomena in diffusive lateral channels, i.e., the inverse spin Hall effect and the spin galvanic effect. A suitable geometry in an applied oblique magnetic field is shown to provide direct access to SOC transport coefficients through a symmetry analysis of the output nonlocal resistance. The scheme is robust against tilting of the spin-injector magnetization, disorder, and spurious non-spin-related contributions to the nonlocal signal and can be used to probe spin-charge conversion effects in both spin-valve and hybrid optospintronic devices.

DOI: 10.1103/PhysRevLett.124.236803

The generation and manipulation of nonequilibrium spins at interfaces are key goals in the operation of spintronic devices, with recent research heavily focused on using SOC for achieving both. As the spin dynamics are sensitive to symmetry-breaking effects, it is conspicuous that transport measurements provide a powerful probe of emergent spin-orbit phenomena. As such, a fundamental understanding of spin transport at interfaces is currently a major enterprise toward the effective control over the spin degree of freedom [1–3].

The conversion of a spin current into a charge current is also essential for an all-electrical readout. SOC has been shown, or predicted, to provide a suitable means to achieve this in several systems with reduced symmetry ranging from two-dimensional (2D) electron gases in oxide-oxide [4], metal-semiconductor [5], and metal-metal [6] interfaces to surface states of topological insulators [7] and spin-split bulk states in polar semiconductors [8]. More recently, heterostructures of 2D crystals have emerged as highly controllable test beds for exploring interfacial SOC phenomena due to their gate-tunable charge carriers and interplay between spin and lattice-pseudospin degrees of freedom [9–13]. This novel class of Dirac materials has further extended the breadth of interfacial phenomena to encompass proximity-induced SOC within atomically thin crystals [14–20], all-optical spin-current injection [21,22], large spin lifetime anisotropy [23–26], and the coexistence of spin Hall effect (SHE) and inverse spin galvanic effect (SGE) [27,28]. Theoretical studies of 2D model systems have also envisioned unconventional spin-orbit scattering mechanisms, including robust skew scattering from spin-transparent impurities [28] and a direct magnetoelectric coupling (DMC) effect—arising from quantum interference between distinct components of the impurity SOC potential—which generates a nonequilibrium spin polarization [29].

The abundance of microscopic spin-orbit mechanisms in materials with broken inversion symmetry has motivated the search for device geometries that can enable electrical detection of spin-charge interconversion effects. The H-bar scheme in Refs. [14,15] employs the SHE for spin-current generation together with its Onsager reciprocal, the inverse SHE (ISHE), for electrical readout. This method can be further extended to the detection of the SGE, the Onsager reciprocal of current-induced spin polarization, as shown in Ref. [30]. However, the two-step process, at the heart of the quadratic dependence of the nonlocal resistance with the spin-charge conversion rate, has serious drawbacks. Primarily, it makes the H-bar approach prone to noise and variability, as demonstrated by the experiments on graphene with adatoms [31–34]. Secondly, it precludes the unambiguous determination of the spin Hall angle (θ_{SHE}) and SGE efficiency (θ_{SGE}) in samples where these effects compete [35–37]. Further progress in this flourishing field will require alternative lateral-device detection schemes where competing SOC effects can be simultaneously detected and quantified.

In this Letter, we propose a measurement protocol for the *unambiguous* linear detection of the ISHE and SGE in lateral spin devices. An optospintronic analog, where the

initial spin accumulation is achieved by purely optical means, is also presented. To illustrate the general principle, we focus on a nonlocal setup comprising a spin injector, a high-fidelity graphene spin channel [38–40], and a cross-shaped junction, where the graphene is covered by a high-SOC material (see Fig. 1). This layout is particularly well suited to the measurement protocol, because one can separate the spin channel from the SOC-active (spin-charge conversion) region. We stress, however, that the detection scheme is *general* to any lateral spin-injection device provided that the breaking of inversion symmetry away from the detection region is sufficiently weak, such that the channel length (L) $\gtrsim$ spin diffusion length (l_s) $\gg$ mean free path (l), which corresponds to the experimentally relevant diffusive regime. As such, the proposed scheme can potentially shed light onto spin-charge conversion effects in different material systems, such as oxide heterostructures [41], metallic bilayers [42], and doped semiconductors [43,44], for which spin injection has been recently established by nonlocal transport methods, but the precise interplay of the ISHE and SGE is yet to be uncovered.

The general principle is akin to electrical detection of the ISHE [45]. Spin-polarized carriers, injected by applying a current I at a ferromagnet (FM) contact, generate lateral charge accumulation via SOC, which is then detected as a nonlocal voltage at the Hall cross. The possibility to isolate SGE and ISHE contributions on the output signal hinges on a fundamental distinction between nonequilibrium spin-polarization density-induced Hall effect and the most familiar spin-current-induced Hall effect. In the former, the component of the diffusive spin accumulation, with the spin moment *collinear* to the propagation direction, generates a transverse charge current $J_i = \epsilon_{ij}\theta_{\rm SGE}\mathcal{J}^j_j$ $(i,j = x,\ y)$, where $\mathcal{J}^a_i$ is the spin-current density in direction i with the spin polarized in a $(a = x,\ y,\ z)$. Conversely, in the ISHE, the spin moment, the spin-current density, and the charge-current density are mutually *orthogonal* such that $J_i = \epsilon_{ijk}\theta_{\rm SHE}\mathcal{J}^k_j$. Here ϵ_{ij} and ϵ_{ijk} are Levi-Civita symbols and summation over repeated indices is implied. Note that the steady-state spin current is linked to the spin polarization in the channel as $\mathcal{J}^a_i = -D_s\partial_i s^a$, where D_s is the diffusion constant (a more accurate definition is given below). The crucial role played by the active polarization channel—out of plane (s^z) for the ISHE and in plane (s^x) for the SGE—is borne out when coherent spin precession is induced by an *oblique* magnetic field normal to the spin-injector easy axis, $\mathbf{B} = (B_x, 0, B_z)$, forcing diffusive spins to undergo ISHE and SGE *simultaneously* (Fig. 1). Oblique spin precession is a powerful probe of spin-relaxation anisotropy [46,47], and here we show that a suitable detection scheme in an applied oblique field provides access to the charge-spin transport coefficients $\theta_{\rm SHE}$ and $\theta_{\rm SGE}$. Our main result is a linear filtering protocol for the ISHE (+) or SGE (−) nonlocal resistance

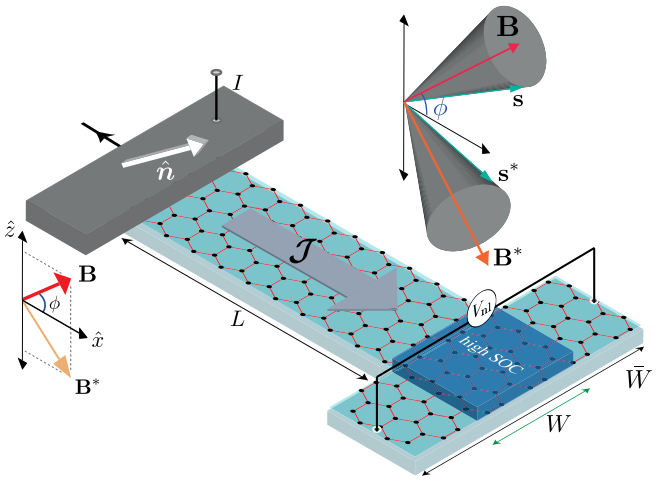

FIG. 1. The injected nonequilibrium spin density $\mathbf{s}$ ($\mathbf{s}^*$) parallel to the FM magnetization $\hat{n} = \mathbf{M}/|\mathbf{M}|$ diffuses through a cross-shaped channel under an applied oblique field $\mathbf{B}$ ($\mathbf{B}^*$). Intrinsic and extrinsic SOC generates a nonlocal voltage ($V_{\rm nl}$).

$$R_{\rm ISHE(SGE)} = \frac{1}{2}[\Delta R_{\rm nl}(\mathbf{B}) \pm \Delta R_{\rm nl}(\mathbf{B}^*)], \tag{1}$$

where $\Delta R_{\rm nl} = (V_{{\rm nl};n_y>0} - V_{{\rm nl};n_y<0})/2I$, with $\hat{n} = \mathbf{M}/|\mathbf{M}|$, is the output transresistance difference between opposite configurations of the spin injector and $\mathbf{B}^* = (B_x, 0, -B_z)$ is the mirror image of $\mathbf{B}$. The spin-charge conversion efficiencies ($\theta_{\rm SHE}$, $\theta_{\rm SGE}$) can be accurately determined using a simple model of the spin-injector magnetization tilting $\mathbf{M}(\mathbf{B})$. (For optical spin injection, the detection is carried out with standard Hanle technique.)

Theory.—We give an intuitive proof of Eq. (1). In the narrow channel limit ($W \ll l_s$), the spin dynamics of a disordered sample with weak SOC ($l_s \gg l$) are well captured by the generalized 1D Bloch model $\partial_t\bar{\mathbf{s}} = D_s\partial_x^2\bar{\mathbf{s}} + \gamma(\bar{\mathbf{s}} \times \mathbf{B}) - \hat{\Gamma}\bar{\mathbf{s}}$ [48], where $\bar{\mathbf{s}} \equiv (\mathbf{s}_{n_y>0} - \mathbf{s}_{n_y<0})/2$ is the spin-density difference between opposite configurations of the spin injector, $\hat{\Gamma} = {\rm diag}\{1/\tau_s^x, 1/\tau_s^y, 1/\tau_s^z\}$, and γ is the gyromagnetic ratio. The spin-relaxation matrix $\hat{\Gamma}$ encapsulates the effects of spin-dephasing [49] and irreversible spin-relaxation mechanisms (which need not be isotropic due to SOC [26]). The output signal $\Delta R_{\rm nl}$ is proportional to the transverse current generated at the cross. A simple dimensional analysis yields $\Delta R_{\rm nl} \propto D_s[\theta_{\rm SHE}\partial_x\bar{s}^z(x) + (\theta_{\rm SGE}/l_s)\bar{s}^x]_{x=L}$. Crucially, since the injected spins follow the contact magnetization, the boundary term satisfies $\bar{\mathbf{s}}(x=0)||\hat{y}$ for any $\mathbf{B}\perp\hat{y}$. This implies that the solution of the 1D Bloch equation for the spin-polarization density *difference* $\bar{\mathbf{s}}$ transforms as $[\bar{s}^x(x), \bar{s}^z(x)] \to [-\bar{s}^x(x), \bar{s}^z(x)]$, under the operation $B_z \to -B_z$. This shows that $\Delta R_{\rm nl}(\mathbf{B}) = \Delta R_{\rm nl}(\mathbf{B}^*)$ for the ISHE and $\Delta R_{\rm nl}(\mathbf{B}) = -\Delta R_{\rm nl}(\mathbf{B}^*)$ for the SGE, thus proving the generality of the filtering scheme of Eq. (1).

We formalize our results with a theory of coupled spin-charge diffusive transport for disordered 2D conductors subject to random SOC sources [50]. The charge and spin observables, coarse-grained over typical distances longer than the mean free path, satisfy the continuitylike equation

$$[\nabla_t s]^a + [\nabla_i \mathcal{J}_i]^a = -\frac{s^a}{\tau_s^a} - \kappa_i^a J_i, \tag{2}$$

the continuity relation $\partial_t \rho = -\partial_i J_i$, and the generalized constitutive relations

$$J_i = -D_c(\partial_i \rho + \kappa_i^a s^a) + \gamma_{ij}^a \mathcal{J}_j^a, \tag{3}$$

$$\mathcal{J}_i^a = -D_s[\nabla_i s]^a + \gamma_{ij}^a J_j. \tag{4}$$

The coefficients appearing in Eqs. (2)–(4) can be obtained from microscopic calculations [50–53]. The DMC efficiency κ_i^a (units m^{-1}) and spin Hall angle γ_{ij}^a quantify the spin-charge conversion efficiency of random SOC sources. In this compact formalism, the effects of spatially uniform spin-dependent interactions are captured by the SU(2) gauge field $\mathcal{A}_\mu = A_\mu^a \sigma^a$ ($\mu = t, i$), with σ^a the spin-1/2 Pauli matrices. The gauge field is implicit in the covariant derivative $[\nabla_\mu O]^a = \partial_\mu O^a \pm \epsilon^{abc} A_\mu^b O^c$, with $O^a = \{s^a, \mathcal{J}^a\}$ a spin observable and the sign $\pm$ holding for a space (+) or time (−) derivative. The time component $A_0^a = g\mu_B B^a$ reproduces the spin precession in the external Zeeman field, and A_i^a encodes the symmetry-breaking SOC [54]. We specialize to uniform SOC of the Bychkov-Rashba (BR) form, which is ubiquitous in interfaces with broken inversion symmetry. For 2D Dirac fermions, its nonzero components read as $A_y^x = -A_x^y = \lambda/v_F$, with v_F the Fermi velocity and λ the BR coupling energy, whereas for parabolic 2D electron gases, $A_y^x = -A_x^y = 2m^*\alpha$, with m^* the effective mass and α the SOC strength. The BR effect contributes to the total spin-charge conversion rates with terms proportional to the momentum scattering time τ, namely, (i) an ISHE-like term $\gamma_{ij}^{a;\mathrm{BR}} = \epsilon_{ij}\omega_{\mathrm{BR}}\tau$, where $\omega_{\mathrm{BR}} = \lambda^2/\epsilon$ with ϵ the Fermi energy (2D Dirac gas) and $\omega_{\mathrm{BR}} = 2m\alpha^2$ (2D electron gas); and (ii) an indirect coupling between spin-polarization density and charge current that modifies the DMC coefficient according to $\kappa_i^a \to \kappa_i^a - \epsilon_{ia}\omega_{\mathrm{BR}}\tau l_R^{-1}$, where $l_R \equiv \hbar/|A_x^y|$ is the length scale of spin precession about the BR field.

With this formalism, we evaluate the spin-density profile in an applied oblique field and establish the range of validity of the linear filtering protocol [Eq. (1)]. Beyond the SU(2) gauge field and impurity scattering, we note that the spin-charge conversion rates can also receive contributions from Berry curvature and phonons [55,56]. For ease of notation, we lump all these contributions under the effective ISHE and SGE rates $\gamma_{ij}^a = \theta_{\mathrm{SHE}}\epsilon_{ij}\delta_{az}$ and $\kappa_i^a = l_{\mathrm{SGE}}^{-1}\epsilon_{ia}$, where δ_{ij} is the Kronecker delta symbol. For disordered samples in the typical weak SOC regime $(\theta_{\mathrm{SGE}}, \theta_{\mathrm{SHE}}) \ll 1$ with $\theta_{\mathrm{SGE}} = l_s/l_{\mathrm{SGE}}$, the buildup of a nonlocal voltage in the cross-shaped device involves two independent steps as described below.

Spin precession and spin-charge conversion.—The effective Bloch equation governing the steady-state spin accumulation is obtained from Eqs. (2)–(4) after eliminating the spin current in favor of the spin-polarization density. To leading order, we find

$$\bar{\boldsymbol{\mathcal{D}}} \cdot \mathbf{s}(x) + \gamma[\mathbf{s}(x) \times \mathbf{B}] = 0, \tag{5}$$

with $\gamma = g\mu_B/\hbar$ and

$$\bar{\boldsymbol{\mathcal{D}}} = D_s \begin{pmatrix} \partial_x^2 - l_{s,x}^{-2} & 0 & \kappa_R \partial_x \\ 0 & \partial_x^2 - l_{s,y}^{-2} & 0 \\ -\kappa_R \partial_x & 0 & \partial_x^2 - l_{s,z}^{-2} \end{pmatrix}, \tag{6}$$

where $l_{s,a} = \sqrt{D_s \tau_s^a}$ ($a = x, y, z$). The diffusion matrix $\bar{\boldsymbol{\mathcal{D}}}$ displays the standard Fick terms (diagonal), accounting for spin-relaxation processes [48], and a conspicuous non-diffusive term proportional to the wavelength of inversion symmetry breaking within the 1D channel $\kappa_R = 2l_R^{-1}$. This term is usually neglected in the analysis of spin precession [48], since it is assumed that the main effect of SOC is a renormalization of spin lifetimes. However, the more general Bloch equation (5) shows that the BR gauge field effectively induces a coherent coupled precession of s_x (SGE) and s^z (ISHE) components as long as $\kappa_R \gtrsim l_s^{-1}$. The protocol, which relies on the decoupling of SGE and ISHE precessions using suitable oblique fields $\mathbf{B}, \mathbf{B}^* \perp \hat{y}$, is essentially exact for $l_R \gg l_s$, since in this limit Eq. (5) reduces to its standard diffusive form. Remarkably, the scheme is still accurate in channels with a moderate to strong BR effect, where l_R can be only a few times larger than l_s; see Supplemental Material [57].

We now turn our attention to the detection region, where SOC generates a transverse current J_y. The nonlocal voltage buildup is determined by the open circuit condition $J_{y,\mathrm{total}} = J_y + (\sigma_{2\mathrm{D}}/\bar{W})V_{\mathrm{nl}} = 0$, where $\sigma_{2\mathrm{D}}$ is the charge conductivity. From Eqs. (3) and (4), we find

$$V_{\mathrm{nl}}(x) = -\frac{\bar{W} D_s}{\sigma_{2\mathrm{D}}}[(\theta_{\mathrm{SGE}}/l_s)s^x(x) + \theta_{\mathrm{SHE}}\partial_x s^z(x)] + \mathcal{O}, \tag{7}$$

where $\mathcal{O}$ are next-order corrections in θ_{SHE} and θ_{SGE}, thus validating the expression of $\Delta R_{\mathrm{nl}}(x)$ obtained earlier via a dimensional analysis argument.

Detection.—We will now show how the detection is carried out in a real setup. We first consider the spin-valve layout in Fig. 1. The injected spin polarization is parallel to the spin-injector quantization axis (defined by $\mathbf{M}$) and, thus, is very sensitive to the applied field [40]. First, a field

$\mathbf{B}_{\rm in} \| \pm \hat{y}$ is applied to set the injector configuration either "up" ($n_y > 0$) or "down" ($n_y < 0$). Subsequently, the field is removed, and an oblique field in the Oxz plane is swept, $\mathbf{B} = (|B|\cos\phi\,\hat{x} + B\sin\phi\,\hat{z})$, across the first and fourth quadrants ($\phi \in [0, 90°]$). The nonlocal resistance difference between opposite configurations of the spin injector, $\Delta R_{\rm nl} \equiv [V_{\rm nl}(L)|_{n_y>0} - V_{\rm nl}(L)|_{n_y<0}]/2I$, is measured and compared to that obtained from Eq. (7) upon solving the effective spin Bloch equation [Eq. (5)] for the spin-density profile $s^a(x)$. After a straightforward calculation, we find

$$\Delta R_{\rm nl} = R_0\,{\rm Im}[e^{-qL}(\theta_{\rm SHE} q l_s s_B \cos\phi - \theta_{\rm SGE}\sin\phi)], \quad (8)$$

where $q = l_s^{-1}\sqrt{1 + \imath B\gamma\tau_s}$ is the complex spin-precession wave vector, $s_B = {\rm sgn}(B)$, and $R_0 = s^y(0)(\bar{W}D_s/l_s I\sigma_{\rm 2D})$. We have also assumed an isotropic spin lifetime $\tau_s^a = \tau_s$, which is characteristic of single-layer graphene [46]. The two contributions in Eq. (8) have opposite parity under mirror reflection $B \to -B$ (or, equivalently, $\phi \to -\phi$). This in turn implies that the bona fide ISHE (+) or SGE (−) spin transresistance satisfies

$$\Delta R_{\rm nl}|^{\mathbf{B}\perp\hat{y}}_{\rm ISHE(SGE)} = \frac{1}{2}(\Delta R_{\rm nl}|_B \pm \Delta R_{\rm nl}|_{-B}), \quad (9)$$

which is simply a special case of Eq. (1). The signal subtraction $\Delta R_{\rm nl} \equiv \frac{1}{2}(R_{\rm nl}|_{n_y>0} - R_{\rm nl}|_{n_y<0})$ ensures that non-spin-related contributions, such as the local Hall effect due to stray fields generated by the FM contact, are filtered out. Moreover, the spin-transresistance scale $R_0 \propto s^y(0) \equiv s^y(0, \mathbf{B})$ defines the maximum achievable nonlocal signal. Contacts with low magnetic anisotropy saturate easily [$R_0 \propto s^y(0, \mathbf{B}) \to 0$ for $B_{x,z} \gg B^{\rm sat}_{x,z}$], which shrinks the $\Delta R_{\rm nl}$ line shape with respect to an ideal spin injector with magnetization pinned along the easy axis $\mathbf{M} \| \pm\hat{y}$. The typical line shapes for an isotropic channel with an ideal contact ($\hat{n} \| \pm\hat{y}$) are shown in Fig. 2(a). For a field applied perpendicularly to the plane ($\phi = 90°$), spins precess in the plane, there is no available out-of-plane spin density, and, thus, the ISHE is absent, while the SGE achieves its highest magnitude. When the field is tilted toward the 2D plane ($\phi < 90°$), a symmetric ISHE component appears. The realistic line shapes are obtained by a trivial rescaling $\Delta R_{\rm nl} \to \mathcal{V}_B \Delta R_{\rm nl}$, where $\mathcal{V}_B = s^y(0, B)/s^y(0, 0)$ is the "visibility" factor that takes into account response of the spin injector [57]. As aforementioned, since $\mathcal{V}_B = \mathcal{V}_{-B}$ (for a homogeneous contact), the only effect of the FM response within the protocol is a shrinkage of the filtered signals. We briefly discuss an alternative detection scheme with an oblique field applied in the Oyz plane [46]. The nonlocal resistance for a fixed spin-injector configuration, $R^{YZ}_{\rm nl} = V^{YZ}_{\rm nl}/I$, is found as

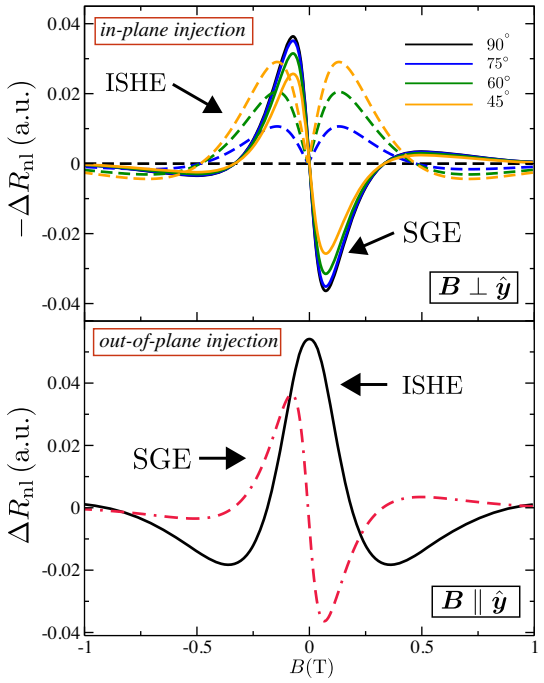

FIG. 2. Detection of ISHE and SGE contributions for in-plane and out-of-plane spin injection. Oblique field parameterized as $\mathrm{B} = |B|\cos\phi\,\hat{x} + B\sin\phi\,\hat{z}$ (see the text for an alternative measurement protocol with $\mathbf{B}\perp\hat{x}$). Plots are for a typical graphene channel ($L = 2l_s$ and $\tau_s = 0.1$ ns) and heterojunction with $\theta_{\rm SHE} = \theta_{\rm SGE} = 0.01$.

$$R^{YZ}_{\rm nl} = r_0[\theta_{\rm SHE}\sin(2\phi)f(q) - \theta_{\rm SGE}\sin\phi\,{\rm Im}\,e^{-qL}], \quad (10)$$

where $r_0 = [s^y(0)]_{\mathbf{B}} \times (\bar{W}D_s/l_s I\sigma_{\rm 2D})$ is the typical transresistance factor and $f(q) = [e^{-L/l_s} - {\rm Re}(q l_s e^{-qL})]/2$. The ISHE and SGE components can be extracted via Fourier analysis if the ϕ dependence of r_0 is known with good resolution. Alternatively, for typical channels ($L \gtrsim l_s$), $\theta_{\rm SHE}$ can be determined directly from nonlocal signal saturation at large field $R^{YZ}_{\rm nl} \to (r_0/2)\theta_{\rm SHE}\sin(2\phi)e^{-L/l_s}$. Once $\theta_{\rm SHE}$ is determined, the SGE coefficient is easily retrievable by fitting the experimental data to Eq. (10).

We now propose an optospintronic analog, in which a transition metal dichalcogenide monolayer replaces the FM contact as a spin injector [12]. Optical spin injection has been recently demonstrated in graphene heterostructures [21,22]. Since optically pumped spin currents from atomically thin semiconductors are polarized normal to the 2D plane, an in-plane field $\mathbf{B} = B\hat{y}$ can be used to detect the ISHE and SGE simultaneously. The opto-spin-transresistance $\Delta R^z_{\rm nl} \equiv [V_{\rm nl}(L)|_{n_z>0} - V_{\rm nl}(L)|_{n_z<0}]/2I$ is easily computed as

$$\Delta R^z_{\rm nl} = r^z_0 {\rm Re}[(q l_s\theta_{\rm SHE} - \theta_{\rm SGE})e^{-qL}], \quad (11)$$

where q is defined as before and $r^z_0 = s^z(0)\bar{W}D_s/(l_s I\sigma_{\rm 2D})$. Similar to the in-plane spin-injection configuration, the ISHE and SGE signals have different parity under

mirror reflection $B \to -B$. Typical line shapes are shown in Fig. 2(b).

Experimental feasibility.—The measurement protocol is directly applicable to devices with anisotropic spin dynamics, e.g., due to the BR effect or spin-valley locking [59]. Different material systems and device layouts can be used provided (i) the injection and detection regions are well separated to avoid the use of large precession fields ($L \gtrsim l_s$) and (ii) the inversion symmetry breaking within the spin channel is weak enough ($l_R \gtrsim l_s$). Such a moderate SOC regime also guarantees that the spin-charge conversion is within the linear regime [Eq. (7)], which is indeed observed for most devices [35–44]. For example, in monolayer graphene, one finds $l_R \approx \hbar v_F/\lambda \approx 14\ \mu\text{m} \gg l_s$ for a typical $\lambda = 50\ \mu\text{eV}$ [60,61]. For interfaces hosting 2D electron gases with a weak or moderate BR effect, the situation is similar. For example, using representative values for the Au(111) surface, $\alpha = 0.03$ eV Å and $m^* = 0.26 m_e$ [62]), one obtains $l_R \approx 100\ \text{nm} \gg l_s$. Beyond this regime, the interpretation of experimental data requires explicit modeling [using a self-consistent solution of Eqs. (2)–(4)], hindering the unambiguous detection of the ISHE and SGE.

We conclude with a remark on the spin-injector magnetization response to the applied field. As shown in this work, the tilting of the magnetization $\mathbf{M}$ away from its preferred easy axis reduces the ISHE or SGE nonlocal resistance by a nonlinear factor (visibility) given by $\mathcal{V}_{\mathbf{B}} = [s^y(0)]_{\mathbf{B}}/[s^y(0)]_{\mathbf{B}=0}$. The field dependence of the initial spin accumulation density $[s^y(0)]_{\mathbf{B}}$ can be accurately described by a Stoner-Wohlfarth model with parameters determined from separate Hanle measurements. According to the realistic simulations provided in Supplemental Material [57], the visibility can be as large as 20% at low fields ~0.1 T for typical FM saturation parameters. We expect that the measurement scheme introduced in this work will enable an accurate experimental determination of spin-charge conversion parameters (θ_{SHE}, $\theta_{\text{SGE}} = l_s/l_{\text{SGE}}$). We note that a similar scheme can, in principle, be employed for electrical detection of the spin Hall effect and Edelstein effect, the Onsager reciprocal phenomena of the ISHE and SGE. For example, this could be achieved by injecting a current perpendicular to the channel and measuring the resulting spin-electrochemical accumulation at the FM contact [63].

In compliance with EPSRC policy framework on research data, this publication is theoretical work that does not require supporting research data.

A. F. gratefully acknowledges the financial support from the Royal Society, London through a Royal Society University Research Fellowship. M. O. and A. F. acknowledge funding from Engineering and Physical Sciences Research Council (Grant No. EP/N004817/1). Y.-H. L., C. H., and M. A. C. acknowledge support from the Ministry of Science and Technology of Taiwan through Grants No. 102-2112-M-007-024-MY5 and No. 107-2112-M-007-021-MY5, as well as from the National Center for Theoretical Sciences (NCTS, Taiwan). C. H. acknowledges partial support from the Army Research Office (Grant No. W911NF-16-1-0472).

*aires.ferreira@york.ac.uk

[1] A. Manchon, H. C. Koo, J. Nitta, S. M. Frolov, and R. A. Duine, New perspectives for Rashba spin–orbit coupling, Nat. Mater. **14**, 871 (2015).
[2] A. Soumyanarayanan, N. Reyren, A. Fert, and C. Panagopoulos, Emergent phenomena induced by spin–orbit coupling at surfaces and interfaces, Nature (London) **539**, 509 (2016).
[3] F. Hellman *et al.*, Interface-induced phenomena in magnetism, Rev. Mod. Phys. **89**, 025006 (2017).
[4] E. Lesne *et al.*, Highly efficient and tunable spin-to-charge conversion through Rashba coupling at oxide interfaces, Nat. Mater. **15**, 1261 (2016).
[5] S. Oyarzún *et al.*, Evidence for spin-to-charge conversion by Rashba coupling in metallic states at the Fe/Ge(111) interface, Nat. Commun. **7**, 13857 (2016).
[6] J. Puebla, F. Auvray, N. Yamaguchi, M. Xu, S. Z. Bisri, Y. Iwasa, F. Ishii, and Y. Otani, Photoinduced Rashba Spin-to-Charge Conversion via an Interfacial Unoccupied State, Phys. Rev. Lett. **122**, 256401 (2019).
[7] J.-C. Rojas-Sánchez *et al.*, Spin to Charge Conversion at Room Temperature by Spin Pumping into a New Type of Topological Insulator: α-Sn Films, Phys. Rev. Lett. **116**, 096602 (2016).
[8] K. Ishizaka *et al.*, Giant Rashba-type spin splitting in bulk BiTeI, Nat. Mater. **10**, 521 (2011).
[9] E. I. Rashba, Graphene with structure-induced spin-orbit coupling: Spin-polarized states, spin zero modes, and quantum Hall effect, Phys. Rev. B **79**, 161409 (2009).
[10] Z. Y. Zhu, Y. C. Cheng, and U. Schwingenschlögl, Giant spin-orbit-induced spin splitting in two-dimensional transition-metal dichalcogenide semiconductors, Phys. Rev. B **84**, 153402 (2011).
[11] D. Xiao, G.-B. Liu, W. Feng, X. Xu, and W. Yao, Coupled Spin and Valley Physics in Monolayers of MoS2 and Other Group-VI Dichalcogenides, Phys. Rev. Lett. **108**, 196802 (2012).
[12] R. A. Muniz and J. E. Sipe, All-optical injection of charge, spin, and valley currents in monolayer transition-metal dichalcogenides, Phys. Rev. B **91**, 085404 (2015).
[13] J. H. Garcia, M. Vila, A. W. Cummings, and S. Roche, Spin transport in graphene/transition metal dichalcogenide heterostructures, Chem. Soc. Rev. **47**, 3359 (2018).
[14] A. Avsar, J. Y. Tan, T. Taychatanapat, J. Balakrishnan, G. K. W. Koon, Y. Yeo, J. Lahiri, A. Carvalho, A. S. Rodin, E. C. T. O'Farrell, G. Eda, A. H. C. Neto, and B. Ozyilmaz, Spin–orbit proximity effect in graphene, Nat. Commun. **5**, 4875 (2014).
[15] Z. Wang, D.-K. Ki, H. Chen, H. Berger, A. H. MacDonald, and A. F. Morpurgo, Strong interface-induced spin–orbit

interaction in graphene on WS2, Nat. Commun. **6**, 8339 (2015).
[16] Z. Wang, D.-K. Ki, J. Y. Khoo, D. Mauro, H. Berger, L. S. Levitov, and A. F. Morpurgo Origin and Magnitude of 'Designer' Spin-Orbit Interaction in Graphene on Semiconducting Transition Metal Dichalcogenides, Phys. Rev. X **6**, 041020 (2016).
[17] T. Völkl, T. Rockinger, M. Drienovsky, K. Watanabe, T. Taniguchi, D. Weiss, and J. Eroms, Magnetotransport in heterostructures of transition metal dichalcogenides and graphene, Phys. Rev. B **96**, 125405 (2017).
[18] B. Yang, M. Lohmann, D. Barroso, I. Liao, Z. Lin, Y. Liu, L. Bartels, K. Watanabe, T. Taniguchi, and J. Shi, Strong electron-hole symmetric Rashba spin-orbit coupling in graphene/monolayer transition metal dichalcogenide heterostructures, Phys. Rev. B **96**, 041409 (2017).
[19] T. Wakamura, F. Reale, P. Palczynski, S. Guéron, C. Mattevi, and H. Bouchiat, Strong Anisotropic Spin-Orbit Interaction Induced in Graphene by Monolayer WS2, Phys. Rev. Lett. **120**, 106802 (2018).
[20] S. Omar and B. J. van Wees, Spin transport in high-mobility graphene on WS2 substrate with electric-field tunable proximity spin-orbit interaction, Phys. Rev. B **97**, 045414 (2018).
[21] Y. K. Luo, J. Xu, T. Zhu, G. Wu, E. J. McCormick, W. Zhan, M. R. Neupane, and R. K. Kawakami, Opto-valleytronic spin injection in monolayer MoS2/few-layer graphene hybrid spin valves, Nano Lett. **17**, 3877 (2017).
[22] A. Avsar, D. Unuchek, J. Liu, O. L Sanchez, K. Watanabe, T. Taniguchi, B Özyilmaz, and A. Kis, Optospintronics in graphene via proximity coupling, ACS Nano **11**, 11678 (2017).
[23] A. W. Cummings, J. H. Garcia, J. Fabian, and S. Roche, Giant Spin Lifetime Anisotropy in Graphene Induced by Proximity Effects, Phys. Rev. Lett. **119**, 206601 (2017).
[24] T. S. Ghiasi, J.-I. Aynés, A. A. Kaverzin, and Bart J. van Wees, Large proximity-induced spin lifetime anisotropy in transition-metal dichalcogenide/graphene heterostructures, Nano Lett. **17**, 7528 (2017).
[25] L. A. Benítez, J. F. Sierra, W. S. Torres, A. Arrighi, F. Bonell, M. V. Costache, and S. O. Valenzuela, Strongly anisotropic spin relaxation in graphene-transition metal dichalcogenide heterostructures at room temperature, Nat. Phys. **14**, 303 (2018).
[26] M. Offidani and A. Ferreira, Microscopic theory of spin relaxation anisotropy in graphene with proximity-induced spin–orbit coupling, Phys. Rev. B **98**, 245408 (2018).
[27] M. Offidani, M. Milletarí, R. Raimondi, and A. Ferreira, Optimal Charge-to-Spin Conversion in Graphene on Transition-Metal Dichalcogenides, Phys. Rev. Lett. **119**, 196801 (2017).
[28] M. Milletarí, M. Offidani, A. Ferreira, and R. Raimondi, Covariant Conservation Laws and the Spin Hall Effect in Dirac-Rashba Systems, Phys. Rev. Lett. **119**, 246801 (2017).
[29] C. Huang, Y. D. Chong, and M. A. Cazalilla, Direct coupling between charge current and spin polarization by extrinsic mechanisms in graphene, Phys. Rev. B **94**, 085414 (2016).
[30] C. Huang, Y. D. Chong, and M. A. Cazalilla, Anomalous Nonlocal Resistance and Spin-Charge Conversion Mechanisms in Two-Dimensional Metals, Phys. Rev. Lett. **119**, 136804 (2017).
[31] J. Balakrishnan, G. K. W. Koon, M. Jaiswal, A. H. Castro Neto, and B. Özyilmaz, Colossal enhancement of spin–orbit coupling in weakly hydrogenated graphene, Nat. Phys. **9**, 284 (2013).
[32] A. A. Kaverzin and B. J. van Wees, Electron transport nonlocality in monolayer graphene modified with hydrogen silsesquioxane polymerization, Phys. Rev. B **91**, 165412 (2015).
[33] Y. Wang, X. Cai, J. R.-Robey, and M. S. Fuhrer, Neutral-current Hall effects in disordered graphene, Phys. Rev. B **92**, 161411R (2015).
[34] T. Völkl *et al.*, Absence of a giant spin Hall effect in plasma-hydrogenated graphene, Phys. Rev. B **99**, 085401 (2019).
[35] C. K. Safeer, J. Ingla-Aynés, F. Herling, J. H. Garcia, M. Vila, N. Ontoso, M. R. Calvo, S. Roche, L. E. Hueso, and F. Casanova, Room-temperature spin hall effect in graphene/MoS2 van der Waals heterostructures, Nano Lett. **19**, 1074 (2019).
[36] T. S. Ghiasi, A. A. Kaverzin, P. J. Blah, and B. J. van Wees, Charge-to-spin conversion by the Rashba-Edelstein effect in two-dimensional van der Waals heterostructures up to room temperature, Nano Lett. **19**, 5959 (2019).
[37] L. A. Benitez, W. S. Torres, J. F. Sierra, M. Timmermans, J. H. Garcia, S. Roche, M. V. Costache, and S. O. Valenzuela, Tunable room-temperature spin galvanic and spin Hall effects in van der Waals heterostructures, Nat. Mater. **19**, 170 (2020).
[38] N. Tombros, C. Jozsa, M. Popinciuc, H. T. Jonkman, and B. J. van Wees, Electronic spin transport and spin precession in single graphene layers at room temperature, Nature (London) **448**, 571 (2007).
[39] M. V. Kamalakar, C. Groenveld, A. Dankert, and S. P. Dash, Long distance spin communication in chemical vapour deposited graphene, Nat. Commun. **6**, 6766 (2015).
[40] M. Gurram, S. Omar, and B. J. van Wees, Electrical spin injection, transport, and detection in graphene-hexagonal boron nitride van der Waals heterostructures: Progress and perspectives, 2D Mater. **5**, 032004 (2018).
[41] N. Reyren, M. Bibes, E. Lesne, J.-M. George, C. Deranlot, S. Collin, A. Barthélémy, and H. Jaffrès, Gate-Controlled Spin Injection at LaAlO3/SrTiO3 Interfaces, Phys. Rev. Lett. **108**, 186802 (2012).
[42] Miren Isasa *et al.*, Origin of inverse Rashba-Edelstein effect detected at the Cu/Bi interface using lateral spin valves, Phys. Rev. B **93**, 014420 (2016).
[43] A. M. Kamerbeek, P. Hogl, J. Fabian, and T. Banerjee, Electric field control of Spin lifetimes in Nb-$SrTiO_3$ by Spin-Orbit Fields, Phys. Rev. Lett. **115**, 136601 (2015).
[44] X. Lou, C. Adelmann, S. A. Crooker, E. S. Garlid, J. Zhang, K. S. M. Reddy, S. D. Flexner, C. J. Palmstrøm, and P. A. Crowell, Electrical detection of spin transport in lateral ferromagnet-semiconductor devices, Nat. Phys. **3**, 197 (2007).
[45] S. O. Valenzuela and M. Tinkham, Direct electronic measurement of the spin Hall effect, Nature (London) **442**, 176 (2006).

[46] B. Raes, J. E. Scheerder, M. V. Costache, F. Bonell, J. F. Sierra, J. Cuppens, J. Van de Vondel, and S. O. Valenzuela, Determination of the spin-lifetime anisotropy in graphene using oblique spin precession, Nat. Commun. **7**, 11444 (2016).

[47] S. Ringer, S. Hartl, M. Rosenauer, T. Völkl, M. Kadur, F. Hopperdietzel, D. Weiss, and J. Eroms, Measuring anisotropic spin relaxation in graphene, Phys. Rev. B **97**, 205439 (2018).

[48] B. Raes, A. W. Cummings, F. Bonell, M. V. Costache, J. F. Sierra, S. Roche, and S. O. Valenzuela, Spin Precession in anisotropic media, Phys. Rev. B **95**, 085403 (2017).

[49] A. W. Cummings and S. Roche, Effects of Dephasing on Spin Lifetime in Ballistic Spin-Orbit Materials, Phys. Rev. Lett. **116**, 086602 (2016).

[50] Y.-H. Lin, C. Huang, M. Offidani, A. Ferreira, and M. A. Cazalilla, Theory of spin injection in two-dimensional materials with proximity-induced spin-orbit coupling, Phys. Rev. B **100**, 245424 (2019).

[51] K. Shen, R. Raimondi, and G. Vignale, Theory of coupled spin-charge transport due to spin-orbit interaction in inhomogeneous two-dimensional electron liquids, Phys. Rev. B **90**, 245302 (2014).

[52] A. A. Burkov, Alvaro S. Núñez, and A. H. MacDonald, Theory of spin-charge-coupled transport in a two-dimensional electron gas with Rashba spin-orbit interactions, Phys. Rev. B **70**, 155308 (2004).

[53] I. V. Tokatly and E. Y. Sherman, Gauge theory approach for diffusive and precessional spin dynamics in a two-dimensional electron gas, Ann. Phys. (Amsterdam) **325**, 1104 (2010).

[54] I. V. Tokatly, Equilibrium Spin Currents: Non-Abelian Gauge Invariance and Color Diamagnetism in Condensed Matter, Phys. Rev. Lett. **101**, 106601 (2008).

[55] J. Sinova, S. O. Valenzuela, J. Wunderlich, C. H. Back, and T. Jungwirth, Spin Hall effects, Rev. Mod. Phys. **87**, 1213 (2015).

[56] C. Gorini, U. Eckern, and R. Raimondi, Spin Hall Effects Due to Phonon Skew Scattering, Phys. Rev. Lett. **115**, 076602 (2015).

[57] See Supplemental Material at http://link.aps.org/supplemental/10.1103/PhysRevLett.124.236803 for additional details on the realistic modeling of ISHE and SGE nonlocal signals in lateral spin-valve devices, which includes Ref. [58].

[58] P. Zhang and M. W. Wu, Electron spin diffusion and transport in graphene, Phys. Rev. B **84**, 045304 (2011).

[59] L. Yang, N. A. Sinitsyn, W. Chen, J. Yuan, J. Zhang, J. Lou, and S. A. Crooker, Long-lived nanosecond spin relaxation and spin coherence of electrons in monolayer MoS_2 and WS_2. Nat. Phys. **11**, 830 (2015).

[60] H. Min, J. E. Hill, N. A. Sinitsyn, B. R. Sahu, L. Kleinman, and A. H. MacDonald, Intrinsic and Rashba spin-orbit interactions in graphene sheets, Phys. Rev. B **74**, 165310 (2006).

[61] S. Konschuh, M. Gmitra, and J. Fabian, Tight-binding theory of the spin-orbit coupling in graphene, Phys. Rev. B **82**, 245412 (2010).

[62] D. Popović, F. Reinert, S. Hüfner, V. G. Grigoryan, M. Springborg, H. Cercellier, Y. Fagot-Revurat, B. Kierren, and D. Malterre, High-resolution photoemission on Ag/Au (111): Spin-orbit splitting and electronic localization of the surface state, Phys. Rev. B **72**, 045419 (2005).

[63] L. Li, J. Zhang, G. Myeong, W. Shin, H. Lim, B. Kim, S. Kim, T. Jin, S. A. Cavill, B. Seo Kim, C. Kim, J. Lischner, A. Ferreira, and S. Cho, Gate-tunable reversible Rashba–Edelstein effect in a few-layer graphene/2H-TaS_2 heterostructure at room temperature, ACS Nano **14**, 5251 (2020).